Three-dimensional magnetic textures in iron oxide nanoflowers

Author: José Manuel Pérez Zegarra, jperezze103@alumnes.ub.edu
Facultat de Física, Universitat de Barcelona, Diagonal 645, 08028 Barcelona, Spain.

Advisors: Adriana Isabel Figueroa Garcia, aifigueroa@ub.edu; Arantxa Fraile Rodríguez, arantxa.fraile@ub.edu

Abstract: A characterization of the three-dimensional magnetization textures in iron oxide nanoflowers is presented. Tomographic reconstructions of synchrotron-based magnetic Transmission X-ray Microscopy images were obtained using precise reconstruction software, from which the texture of 34 individual particles was identified, described and categorized using geometrical and topological parameters. Four texture families were distinguished based on the morphology of the magnetization streamlines, and their robustness was tested interpreting the topological charge Q as an effective Hopf index. Furthermore, Q was established as a strong indicator of the inner magnetization structure. An apparent tendency in magnetization orientation was identified, linking the observed textures to the preferred crystalline orientations of the domains reported in previous works.
Keywords: Iron Oxide Nanoparticles, Superferromagnetism, Tomography, Vortices, Topology, Magnetic textures
SDGs: Goal 3, Good health and wellbeing; Goal 6, Clean water and sanitation

I. INTRODUCTION

Iron oxide nanoflowers (NFs) made of maghemite ($\gamma - Fe_2O_3$) have been a central topic of research due to their potential application in environmental remediation and biomedical diagnosis and treatment [1]. They are flower-like due to their core-aggregation structure, which arranges the different domains (cores) in an almost spherical shape, as seen by High Resolution Transmission Electron Microscopy (HRTEM) images (see Fig. 1 (a)). During their synthesis, the NFs form aggregates that can be regarded as hierarchical magnetic nanostructures, as three distinct levels of magnetic order are observed (ferrimagnetic, superferromagnetic and supraferromagnetic) [1, 2]. In order to uncover the magnetic textures underlying this hierarchy, some magnetism groups have investigated dispersed aggregates of NFs, such as the NF200 sample studied in this work, where individual NFs can be isolated using proper imaging techniques [1].

The NF200 sample was synthesised through polyol routes in the group of M. Puerto Morales at ICMM-CSIC (see Ref. [1] and references therein). Afterwards, the Magnetic Nanomaterials Group (MNG) at the UB dispersed the NFs in organic solvents and deposited them onto C-coated Cu TEM grid membranes for the synchrotron-based X-ray transmission microscopy (TXM) experiments. The NF200 sample consists of nanoflowers with a mean size of 186 ± 28 nm and cores of 20 ± 4 nm, exhibiting a remanent magnetization (M_r) of 5.3 ± 0.5 emu/g Fe_2O_3 [1].

The effective superferromagnetism of the sample resulted from highly correlated internal configurations, modulated by exchange energies, which led to magnetization states with $M_r \approx 0$. This idea was reinforced after initial experiments of the magnetic textures for individual NFs, using TXM combined with X-ray magnetic circular dichroism (XMCD). Using these 2D magnetization maps, three types of magnetic textures were initially identified [1]: vortex-like structures, particles with 2 regions of almost homogeneous magnetization, and NFs with intermediate structures. Near zero magnetization value for all configurations was found and no link between size and demagnetization was observed. Micromagnetic simulations confirm that the interplay between inter-core exchange and demagnetizing fields stabilizes a partially topologically protected vortex-like spin state at low fields [1].

Given the large diversity of magnetic textures obtained from the NF200 sample, open questions remained regarding the nature of these configurations: how are the vorticity structures distributed within a single NF? Does a 3D image of the magnetic texture provide further insights into the NFs magnetic behaviour?

To address these questions, full 3D tomographies were recorded, based on TXM images recorded at different angles at the MISTRAL beamline of the ALBA synchrotron. This work aims to advance the characterization of 3D magnetic structures by combining experimental data with newly developed analysis tools. Given the limited literature on true 3D magnetic imaging, this study offers a systematic classification of 3D magnetic configurations in nanostructures based on key magnetization and topological parameters.

II. METHODOLOGY

All the data studied in this work correspond to a series of synchrotron-based X-ray magnetic tomograms for the NF200 sample. XMCD images were acquired at the resonant L_3 absorption edge, $E = 711$ eV, that yields maximum XMCD contrast for right- and left-circularly polarized light. The sample was measured in remanence, after the application of an almost saturating 0.2 T out-of-plane external field. Tomographies were prepared for $\theta = -50°$ to $+45°$ in steps ranging from $1°$ to $3°$ (rotation around in-plane y axis), for the two azimuthal rotations ($\phi = 0°$ and $90°$) (rotation around out-of-plane z axis).

Image reconstruction of the 3D magnetic textures in

the NFs used an open-source software for synchrotron-radiation-based magnetic tomographies [3, 4]. It comprises two user-friendly *MATLAB* GUIs for *Isolation* and *Analysis*, which allow for imaging each NF. Small modifications were implemented to the code to make this process reproducible and more sensitive to secondary vorticity regions, as described below.

The first step of the processing consists in isolating a single NF from the image, which was generally a difficult task, since the particles often appeared in aggregates (see labels in Fig. 1 (b)-(d)). Only particles without overlap could be studied with certain precision, limiting this study to 34 in total, and not the hundreds visible in the images for the NF200. A threshold was then defined, removing all pixels with contrast below it and generating a 3D array of cubic voxels — with embedded magnetization vectors — resembling the NF. Although this might seem a critical parameter, it proved largely insensitive: any value ensuring sufficient contrast along the z-axis produced identical masks, likely due to the much stronger particle signal compared to the background. Next, a rectangular cut was made to isolate the particle, wide enough in both x–y and x–z planes to visualize its magnetic interaction with neighboring structures. A second GUI then enabled a finer cut, allowing the user to precisely delimit the NF with the cursor.

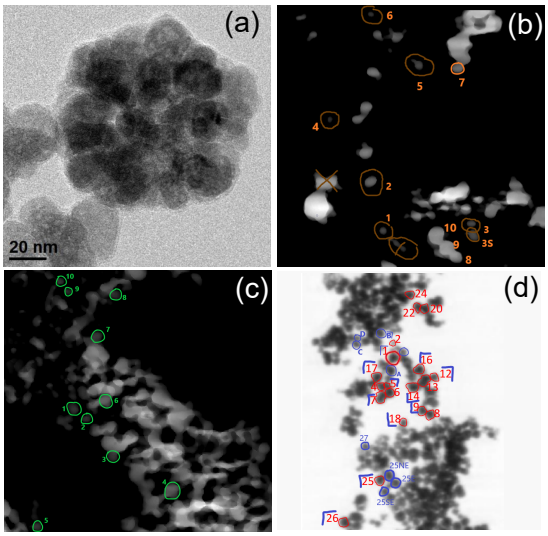

FIG. 1: (a)-(c) Indexation of particles analyzed on Regions I, II and III of the sample respectively. (d) HRTEM image of a particle from the NF200 sample. Note the almost spherical shape and the small cores attached to the neighbour.

The first part of the analysis included an ellipsoid fit for the particle, as well as a decomposition of the total magnetization of the particle, averaging the **m** vector of the whole structure. In the next step, the highest vorticity region was localized and also fitted to an ellipsoid, which yielded the location of the vorticity centre. It also showed the centroid and volume of the four highest vorticity regions. That information is highly useful for the last stage, where the topological charge Q, that will be defined below, was calculated. Here, the program used a function to calculate Q along the three principal axes, indicating a radius for the integration sphere. For structures in which the vorticity centre did not coincide with any of the principal axis, the calculation of Q was performed by manually specifying the coordinates of the centre in the analysis tool. Once this process was done, a new .vtk file was saved, including also an emergent field (B_e) vector field which helped to discover hidden high-Q, looking at sources of this vector field in the open software ParaView (6.0.1 version) [6]. Finally, the 3D reconstruction files generated after saving the narrow and broad masks were analysed. Magnetic structures were constructed by representing magnetization streamlines (see Fig. 2(a)). These represent the integral curves of the magnetization vector field and constitute a key element of this procedure, as they provide a qualitative visualization of the extended internal magnetic textures. To improve the Q calculations made in the GUI program, B_e streamlines were also represented (see Fig. 2(b)). It is worth mentioning the limitations encountered using this reconstruction method. First, the pixel resolution was low (between 8.34 and 8.67 nm for the different images). Although these effects were partially mitigated by the sub-pixel interpolation made during the reconstruction, the tilt-induced geometrical distortion (dependent on the distance to the rotation axis) could not be reliably estimated due to the limited spatial resolution and the absence of a full angular tomographic reconstruction (not θ limited). Secondly, the masks were built from a series of 2D images with limited θ-range, which led to a strong missing wedge effect. This procedure elongated the particle (and its magnetization) in the z direction introducing also a mix between the x and z coordinates (producing a false vorticity in the $x-z$ plane) given by the incorrect association of transmission attenuation with rotational effects [3].

Inevitably, the criteria used were highly subjected to human bias. For example, the final isolation of the particle was a manual cut around the contrast centre. Thus, any conclusions regarding the shape and size of these NFs have to be taken with caution, as higher spatial resolution is needed for a robust morphological analysis. Neither should these measurements be expected to agree with the average diameter parameter for the whole sample ($d = 186 \pm 28\ nm$), since non-aggregated particles might have different size. However, it is worth remarking that these limitations have minimal effect on one of the key parameters of this study: the topological charge.

III. DATA ANALYSIS

A. Topological charge Q

The topological charge, Q, is a parameter used to describe consistently the type and stability of magnetic textures that are held in a magnetic material. It was com-

puted using the following expression:

$$Q = \frac{1}{8\pi} \int \epsilon_{ijk} \mathbf{m} \cdot \partial_j \mathbf{m} \times \partial_k \mathbf{m} \, \mathrm{d}A_i = \frac{1}{4\pi} \int q_i \, \mathrm{d}A_i \quad (1)$$

The integral is evaluated over a closed surface, where $\mathbf{m}$ denotes the normalized magnetization vector, which can be mapped onto the unit sphere S^2. The quantity Q characterizes how the magnetization twists and varies over this surface and, as discussed below, reflects the internal linking of the magnetic structure.

From the surface integral in Eq. 1, the integrand

$$q_i = 1/2 \cdot (\epsilon_{ijk} \mathbf{m} \cdot \partial_j \mathbf{m} \times \partial_k \mathbf{m}) \quad (2)$$

defines the topological charge density, which locally describes how infinitesimal surface elements are mapped onto the unit sphere S^2. The emergent field associated with the topological charge is defined as $B_e = \hbar q_i$. Crucially, this quantity can be extended into the bulk, in analogy with Gauss's theorem for electric charge, $Q = \frac{1}{4\pi} \int_V \nabla \cdot q_i \; dV$. Since Q obeys a Gauss-like law, it is expected to be conserved as long as its source remains enclosed within the integration volume. The difficulty arises from the fact that Q, and even its charge density q_i, are not precisely localized in space, unlike electric charge. From its definition in Eq. 2, it depends on the cross product of two $\mathbf{m}$ derivatives, so its value is entirely determined by the surrounding magnetization texture. Therefore, to understand the invariance of Q, one must characterize the types of configurations that give rise to a non-trivial topological charge and explain how $\mathbf{m}$ can be deformed while preserving the same Q value. This is naturally addressed within the framework of topology.

In magnetism, topologically protected textures are described as (continuous) knots (vorticity regions) in $\mathbf{m}$, which cannot be dissolved using continuous deformations. This can only be cleared by singularities or discontinuities (high-energy electric/magnetic fields and thermal excitations) or changing the space basis (physical partitions of the structure). However, a precise topological classification of these textures requires well-defined boundary conditions and appropriate compactification of the system. In that case, Eq. 1 would define a genuine Hopf invariant, equivalent to the Hopf index $H = Q$.

In the present system, these conditions are not strictly fulfilled. This is partly due to the finite experimental volume and the limited angular reconstruction, but more precisely, due to the non-uniformity of $\mathbf{m}$ in the boundaries of the masks; there is no global periodicity or asymptotic reference state. Hence, Q is treated as a sort of effective Hopf index, which captured the essential topological features of the observed magnetic textures.

Connecting H (and Q) to different textures is a difficult task, since H index is more complex than the 2D winding number $n = \frac{1}{4\pi} \int_S \mathbf{m} \cdot \partial_x \mathbf{m} \times \partial_y \mathbf{m} \, \mathrm{d}x \, \mathrm{d}y$. Essentially, adding one dimension introduces the possibility of wrapping/linking different textures together, so a new interpretation is needed, where H is analysed in terms of the linking of different flux tubes. That is formally discussed in Ref. [7], where it is shown that non-integer H can only be described by studying the self-linking and inter-linking of flux tubes of B_e in systems with mixed topology. These systems have mutually linked tubes that are mixed with extended or open field structures, which break the ideal single uniform state at the boundary. In that context, they introduce that *mixing* via periodic boundary conditions along a direction z and use that axis to define a background magnetization as a reference state. In the present case, the remnant field might be associated with the remnant magnetization after saturation or the preferred $\mathbf{m}$ configurations defined by the NF crystals.

B. Extracted Observables & Texture Classification

Several parameters were extracted for 34 NFs, however, only the three most relevant, namely diameter d, magnetization direction $\mathbf{m} = (m_x, m_y, m_z)$, and Q, are discussed in the following, as they exhibit correlations and enable the categorization of the magnetic textures (see full list in Table II in the Appendix).

First, 34 NFs were selected based on the continuity of magnetization streamlines and vorticity regions, to ensure that each analysed volume corresponded to a single, isolated particle. Second, on the ellipsoidal shape of the mask, expected to approximate a sphere, as inferred from HRTEM images, and providing an estimate of how well isolated the particles are. Lastly, and most importantly, on the replicability of Q for slightly different masks, which adds robustness to the study, as described in the previous section.

Following the criteria described above, the magnetic textures were classified as: (A), isolated/closed vortices; (B), near uniform domains; (C), connected vortices; (D), bifurcations. Representative examples of the reconstructed magnetic textures for NFs in each family are shown in Fig. 2. Types A and B agree well with some already described in Ref. [1]. These families were defined based on the morphology of the magnetization field within a volume defined by a mask. This mask typically covered most of the NF; however, in some cases, it covered only a fraction of it or even included a neighbouring NF, particularly when the magnetization escaped through the particle boundaries, as was especially observed in type C textures.

Type A textures correspond to isolated vortices, in which the magnetization closes around a well-defined vorticity core. In this case, the streamlines do not escape to neighbour textures but remain self-contained within a single NF, following the background magnetization. Type B refers to regions of nearly-uniform magnetization, or to zones where two such domains merge, often giving rise to streamlines with a slight U-shaped curvature at the NF borders. However, these regions do not support a well-defined topology and yield low values of Q. Type C (connected vortices) comprise vortices that couple to

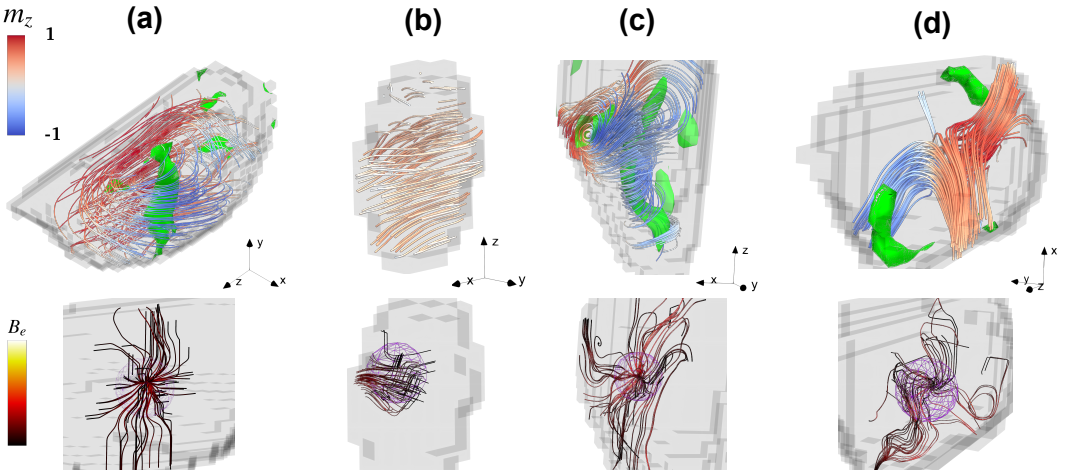

FIG. 2: Representative examples of 3D magnetic textures in iron oxide nanoflowers: (a) Type A, (b) Type B, (c) Type C, and (d) Type D. The textures are categorized based on the continuity of magnetization streamlines and its connectivity to vorticity regions. The top row shows **m** streamlines and vorticity regions (green isosurfaces). The bottom row shows B_e (magnitude) integration lines below each corresponding structure, computed from an integration sphere shown in purple.

other vorticity centres, with streamlines escaping from one core toward others, which may even belong to neighboring NFs. Finally, type D corresponds to regions where **m** splits into 3 or more branches, forming Y-shaped or star-like configurations that define multiple flux tubes diverging from the integration volume. Similar branching patterns have been reported in three-dimensional layered magnetic nanostructures, where they are interpreted as incomplete or precursor topological states rather than stable Hopf textures [5].

The topological charge Q was calculated within the same integration volume used for the morphological classification, correlating texture morphology with topological properties. While types A–C were categorized by based on initial visual inspection, the method was reciprocal for type D textures; these were identified by locating high-Q regions, which subsequently revealed their unique morphological characteristics.

IV. RESULTS AND DISCUSSION

Using the data from Table **??** in the Appendix, scatter plots of Q as a function of both the average NF diameter and the texture family are shown in Fig. 3 (a). In addition, a boxplot is included, separating three size groups—small, medium and large—according to the minimum and maximum registered values of the diameter d. Remarkably, fractional values of Q are dominant in this study and take higher values for the largest particles, which can host more complex structures. However, Q cannot be regarded solely as a measure of twist. As discussed above, an effective Hopf index H quantifies connection between different fluxes of emergent magnetic field, which may circulate around a single vorticity centre or around different ones. Thus, Q is expected to be determined by the linking between the various B_e flux tubes and the background magnetization texture.

Lower Q values in the range of $0 \lesssim Q \lesssim 0.4$ were frequent in type A (7 out of 14) and B (8 out of 10) textures, as shown in Fig 3 (b). Near-zero values were obtained for near-uniform domains (type B). Nearly ideal vortices with a well-defined, almost uniform vorticity core typically exhibited $Q \sim 0.2$. These vortices showed little torsion of **m**, so that the emergent field B_e did not form closed or converging flux tubes capable of linking (see Fig. 2 (b)). Higher Q values within this range corresponded to U-shaped structures captured in the blend between domains.

Higher Q values, $0.4 \lesssim Q \lesssim 1.0$, were dominant in texture type A (7 out of 14), type C (5 out of 7) and type D (8 out of 8, partially by construction bias). Isolated vortices with larger Q were present in NFs that covered a broad range of orientations and wrapped globally in three dimensions, enabling inter-linking of the emergent field B_e across the particle, i. e., preventing the texture from being continuously deformed into a uniform trivial state. When displayed, these structures presented strong convergence or divergence of B_e within the integration volume, a signature of non-local flux linking and incomplete topological closure (see Fig. 2 (a), (c), (d)).

The uncertainty associated with the evaluation of Q was not considered in the previous discussion, as it does not affect the statistical trends. The uncertainty ΔQ arises mainly from the definition of the integration volume and the discretization of the magnetization, and was estimated as $\Delta Q \approx 0.1$, based on the variation of Q for different integration centres and sizes. Larger variations were found for type D structures or lateral vortices in type B textures, corresponding to partially developed configurations, where the associated magnetization fluxes are not fully enclosed within a single region.

To identify orientation preferences of **m**, scatter and boxplots of the m_x, m_y and m_z components were gener-

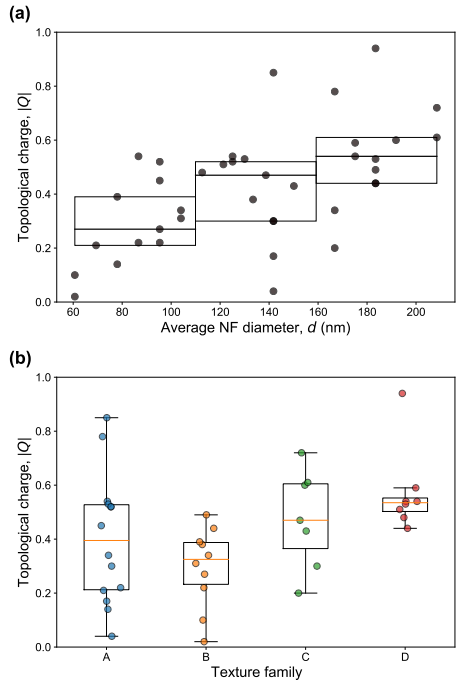

FIG. 3: (a) Absolute topological charge $|Q|$ as a function of average diameter d, with boxplots representing small, medium, and large NF size groups. The uncertainty in d, dominated by the voxel resolution ($\sim 8\,nm$), is small compared to the symbol size. (b) $|Q|$ values categorized by texture family (A, B, C, and D) with jittered points.

ated (see Fig. 4 in the Appendix). The statistical analysis shows $m_y = -0.40 \pm 0.20$ (95% confidence interval (CI)), indicating a preference for negative y values since 0 lies outside this CI. In contrast, m_x and m_z components are more dispersed and centred around zero, with a slight tendency towards positive values. Since this trend is present for both isolated and clustered NFs, the preferred axis along y might be stabilized not only by the supraferromagnetic effects of the superstructures [2], but also by the intrinsic crystalline structure, which might favour the formation of vortices with $-y$ polarization. This aligns with the findings of Ref. [1], where a strong preferential crystalline orientation was found by electron diffraction. Thus, the net axial polarization may reflect not only the history of the applied magnetic field but also a significant contribution from the internal anisotropy of the NF.

V. CONCLUSIONS

A systematic analysis of the 3D magnetic textures in iron oxide nanoflowers was carried out using an open-source software for the processing and reconstruction synchrotron-radiation-based magnetic tomographies. Four distinct texture families were identified through a combined analysis of magnetization field geometry and topological charge Q calculations, capturing both visually apparent and topologically distinct structures. Despite the limited inherent image resolution, an apparent correlation emerged between the morphology of each texture family and the topological charge Q calculated in the same region. Contrary to initial expectations, vortex-like families presented also low Q values, particularly for vortices with little torsion (weak linking between emergent flux tubes) and small diameters, where $\mathbf{m}$ has less room to vary. High Q values were common in families A, C and D, corresponding to configurations that were visibly not self-contained, such as the unexpected bifurcations. These cases exhibited unusual high Q values and occasionally coexisted with vortex cores, in agreement with other works which suggest bifurcation as vortex precursor states. Finally, a preferred orientation of $\mathbf{m}$ was unveiled for NFs both in aggregates and as isolated particles. This finding is in agreement with the previously-reported preferred direction of the crystalline domains that build each NF.

Acknowledgments

I would like to thank my supervisors Adriana and Arantxa for their mentorship and motivation. I'm also grateful to Estela for her unwavering support during the software training. Finally, I extend my deepest thanks to my parents, my grandparents and my friends for their constant support throughout my academic journey.

[1] C. Moya, M. Escoda-Torroella, J. Rodríguez-Álvarez, et al., *Unveiling the crystal and magnetic texture of iron oxide nanoflowers*, Nanoscale **16**, 1942-1951 (2024).
[2] P. Bender, D. Honecker, and L. Fernández, *Supraferromagnetic correlations in clusters of magnetic nanoflowers*, Appl. Phys. Lett. 115, 132406 (2019).
[3] A. E. Herguedas Alonso, *Experimental micromagnetism by vector magnetic tomography*, PhD Thesis, University of Oviedo, Chapter 3 (2025).
[4] A. E. Herguedas Alonso, J. Gómez, C. Fernández, et. al., *MARTApp: software for the processing and reconstruction of synchrotron-radiation-based magnetic tomographies*, Journal of Synchrotron Radiation **32**, Part 4, 1095-1104 (2025).
[5] A. Hierro-Rodriguez, C. Quirós, A. Sorrentino, et al., *Revealing 3D magnetization of thin films with soft X-ray tomography: magnetic singularities and topological charges*, Nature Communications **11**, 6382 (2020).
[6] Ahrens, James, Geveci, et. al., *ParaView: An End-User Tool for Large Data Visualization*, Visualization Handbook, Elsevier, ISBN-13: 9780123875822 (2005)
[7] M. Azhar, S. C. Shaju, R. Knapman, et al., *3D Magnetic Textures with Mixed Topology: Unlocking the Tunable Hopf Index*, arXiv:2411.07722 [cond-mat.mes-hall] (2024).

Textures magnètiques tridimensionals en nanoflors d'òxid de ferro

Author: José Manuel Pérez Zegarra, jperezze103@alumnes.ub.edu
Facultat de Física, Universitat de Barcelona, Diagonal 645, 08028 Barcelona, Spain.

Advisors: Adriana Isabel Figueroa Garcia, aifigueroa@ub.edu; Arantxa Fraile Rodríguez, arantxa.fraile@ub.edu

Resum: Es presenta una caracterització de les textures de magnetització tridimensionals en nanoflors d'òxid de ferro. Es van obtenir reconstruccions tomogràfiques magnètiques d'imatges de microscòpia de transmissió de raigs X de sincrotró, mitjançant programari especialitzat de reconstrucció, a partir de les quals es va identificar, descriure i categoritzar la textura de 34 partícules individuals utilitzant paràmetres geomètrics i topològics. Es van distingir quatre famílies de textures basades en la morfologia de les línies de flux de la magnetització, i se'n va provar la robustesa interpretant la càrrega topològica Q com un índex de Hopf efectiu. A més, Q es va establir com un indicador sòlid de l'estructura interna de la magnetització, fins i tot amb la resolució limitada de les imatges disponibles. Es va identificar una tendència aparent en l'orientació de la magnetització, que vincula les textures observades amb les orientacions cristal·lines preferents dels dominis descrites en treballs previs.
Paraules clau: Nanoflors d'Òxid de Ferro, Superferromagentisme, Tomografies, Vòrtex, Topologia, Textures Magnètiques
ODSs: Aquest TFG està relacionat amb els Objectius de Desenvolupament Sostenible 3 i 6.

Objectius de Desenvolupament Sostenible (ODSs o SDGs)

1. Fi de la es desigualtats		10. Reducció de les desigualtats	
2. Fam zero		11. Ciutats i comunitats sostenibles	
3. Salut i benestar	X	12. Consum i producció responsables	
4. Educació de qualitat		13. Acció climàtica	X
5. Igualtat de gènere		14. Vida submarina	
6. Aigua neta i sanejament		15. Vida terrestre	
7. Energia neta i sostenible		16. Pau, justícia i institucions sòlides	
8. Treball digne i creixement econòmic		17. Aliança pels objectius	
9. Indústria, innovació, infraestructures			

Aquest treball està alineat amb els ODS 3 i 6, ja que les nanopartícules en estudi tenen potencials aplicacions en oncologia i en el sanejament d'aigües.

Appendix A: Table with the observable paramteres of the 34 NFs

TABLE I: Geometrical and magnetic parameters of the analysed nanoflowers (NFs). NF Label indicates the particle indexation for PI#, PII#, and PIII# corresponding to images I, II, and III shown in Fig. 1. PX#*(i) rows indicate the particles represented at (i) in Fig. 2,. P.A. 1, P.A. 2 and P.A. 3 correspond to the lengths (in pixels) of the principal axes obtained from an ellipsoidal fit of each NF. The average diameter d is reported in nanometres, by averaging the pixel diameter in the $x-y$ tomographies shown at Fig. 1 and multiplied by the pixel resolution (8.34 nm for image I, and 8.67 nm for images II and III). Q denotes the topological charge calculated within the selected integration volume. Texture Family refers to the morphological classification. (m_x, m_y, m_z) are the components of the averaged magnetization direction. The last column indicates whether the NF is isolated (I) or part of a cluster (C). While parameters such as magnetization modulus and total volume were initially computed, they were excluded to maintain the robustness of the results, as mask-dependent discrepancies increased considerably during error propagation.

NF Label	P.A. 1 (pix)	P.A. 2 (pix)	P.A. 3 (pix)	d (nm)	Q	Texture	m_x	m_y	m_z	Isolated/Clustered
PI 18	32.6	19.1	17.3	150.12	0.43	C	-0.069	-0.881	0.468	C
PI 17	45.0	22.0	21.0	175.14	0.59	D	-0.186	-0.978	-0.095	C
PI B	40.0	18.0	17.0	141.78	0.30	C	0.864	-0.123	-0.488	C
PI 1	55.0	24.0	23.0	191.82	-0.60	C	-0.450	-0.830	0.330	C
PI 25	41.3	24.5	20.2	125.10	-0.52	A	-0.120	-0.570	0.810	C
PI 25E	44.6	18.2	17.4	141.78	0.17	A	0.300	-0.660	0.670	C
	44.6	18.2	17.4	141.78	0.04	A	0.300	-0.660	0.670	C
PI 25NE*(a)	43.0	21.6	20.0	166.80	0.78	A	-0.120	-0.220	0.970	C
PI 25SSE	32.0	19.6	14.9	125.10	0.54	A	0.040	-0.860	0.560	C
PI 25SE	33.7	18.6	17.3	141.78	0.30	A	0.160	-0.810	0.570	C
PI A	41.3	21.3	19.7	166.80	0.20	C	0.110	-0.890	0.440	C
PI 12	38.9	18.6	16.7	141.78	0.85	A	0.450	0.260	-0.850	C
PI 7	43.8	24.3	18.8	175.14	0.54	D	0.130	-0.870	0.460	C
PI 8	48.4	24.1	20.8	183.48	0.44	B	0.020	-0.810	0.580	C
PI 9	43.1	23.4	20.9	183.48	-0.49	B	-0.020	-0.940	0.320	C
	43.1	23.4	20.9	183.48	0.44	D	-0.020	-0.940	0.320	C
PI 27	31.6	17.1	15.1	133.44	0.38	B	0.280	-0.940	0.170	C
PI 16	48.9	20.4	20.3	166.80	0.34	A	0.420	-0.750	0.500	C
PI 14	48.5	24.4	21.2	183.48	-0.53	D	0.190	-0.920	0.330	C
	48.5	24.4	21.2	183.48	0.94	D	0.190	-0.920	0.330	C
PI 13	58.1	32.0	22.5	208.50	-0.72	C	-0.090	-0.370	0.930	C
	58.1	32.0	22.5	208.50	0.61	C	-0.090	-0.370	0.930	C
PII 1	17.9	10.3	9.7	86.67	0.54	D	-0.140	-0.980	-0.150	I
PII 2	27.4	17.7	13.0	130.01	0.53	A	-0.220	-0.900	0.380	I
PII 3	18.7	12.6	9.0	95.34	0.27	B	0.750	0.450	0.490	I
PII 3S	20.2	16.2	11.9	112.67	0.48	D	0.640	0.620	-0.440	I
PII 5	18.7	12.9	11.2	104.00	0.34	B	0.890	-0.410	0.190	I
	18.7	12.9	11.2	104.00	0.31	B	0.890	-0.410	0.190	I
PII 6*(b)	13.1	7.8	6.6	60.67	0.10	B	-0.590	0.710	0.380	I
PII 7*(d)	30.0	15.5	13.0	121.34	-0.51	D	0.870	-0.430	0.260	C
PIII 1	20.7	12.2	10.7	95.34	0.52	A	0.150	-0.340	0.920	I
PIII 2	19.3	10.0	8.2	78.00	0.39	B	0.530	-0.840	-0.010	I
PIII 3	24.1	11.8	11.6	95.34	-0.45	A	0.890	0.440	0.080	C
PIII 4*(c)	41.1	17.5	15.7	138.67	0.47	C	-0.900	0.300	-0.300	C
PIII 5	23.4	9.8	8.1	78.00	0.14	A	-0.570	-0.700	0.440	I
PIII 7	24.1	12.2	10.4	95.34	0.22	A	0.110	0.950	0.290	C
PIII 8	20.2	10.8	9.4	86.67	0.22	B	0.970	-0.170	0.180	C
PIII 9	19.1	7.7	7.0	60.67	0.02	B	0.420	0.700	0.570	I
PIII 10	21.5	9.2	7.6	69.34	0.21	A	0.470	-0.880	-0.070	I

Appendix B: Orientation preferences

TABLE II: Statistical analysis of the averaged magnetization components over the analysed nanoflowers.

Component	Average μ	Std. Dev. σ	95% CI	N
m_x	0.18	0.46	±0.15	34
m_y	-0.40	0.60	±0.20	34
m_z	0.29	0.41	±0.14	34

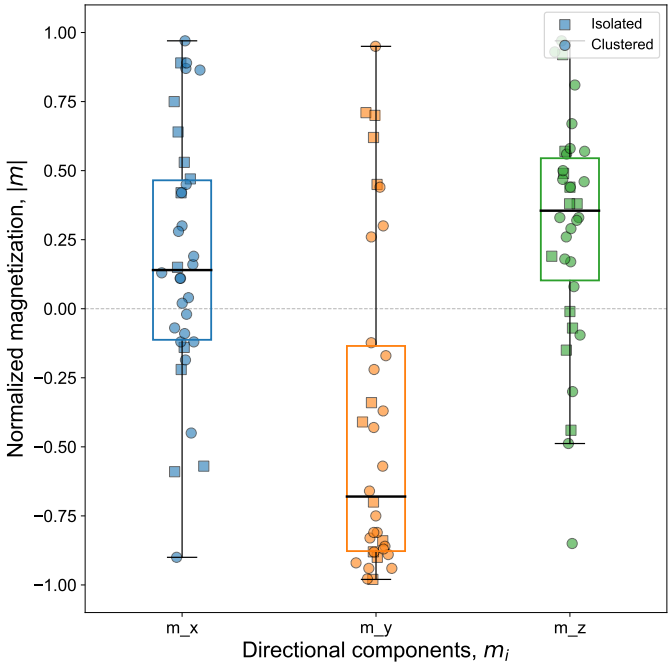

FIG. 4: Scatter plot overlapped by a box-plot of the m_x, m_y and m_z magnetization components. Isolated particles are plotted as square points, while clustered NFs are circles. No preference is observed for any of the two types, suggesting that the y-axis anisotropy has an internal origin.